Taylor & Francis
Taylor & Francis Group

A high-throughput lysosome trafficking assay guides ligand selection and elucidates differences in CD22-targeted nanodelivery

Hannah J. Vaughan[a], Savannah Est-Witte[a], Lance T. Dockery[a], Morgan A. Urello[a], Jonathan Boyd[b], Brittany D. Keyser[a], Li Zhuang[a], Marcello Marelli[a] and R. James Christie[a]

[a]Biologics Engineering, Oncology R&D, AstraZeneca, Gaithersburg, MD, USA;
[b]Discovery Sciences, BioPharma R&D, AstraZeneca, Gaithersburg, MD, USA

ABSTRACT

Targeted nanoparticles offer potential to selectively deliver therapeutics to cells; however, their subcellular fate following endocytosis must be understood to properly design mechanisms of drug release. Here we describe a nanoparticle platform and associated cell-based assay to observe lysosome trafficking of targeted nanoparticles in live cells. The nanoparticle platform utilizes two fluorescent dyes loaded onto PEG-poly(glutamic acid) and PEG-poly(Lysine) block co-polymers that also comprise azide reactive handles on PEG termini to attach antibody-based targeting ligands. Fluorophores were selected to be pH-sensitive (pHrodo Red) or pH-insensitive (Alexafluor 488) to report when nanoparticles enter low pH lysosomes. Dye-labelled block co-polymers were further assembled into polyion complex micelle nanoparticles and crosslinked through amide bond formation to form stable nano-scaffolds for ligand attachment. Cell binding and lysosome trafficking was determined in live cells by fluorescence imaging in 96-well plates and quantification of red- and green-fluorescence signals over time. The platform and assay was validated for selection of optimal antibody-derived targeting ligands directed towards CD22 for nanoparticle delivery. Kinetic analysis of uptake and lysosome trafficking indicated differences between ligand types and the ligand with the highest lysosome trafficking efficiency translated into effective DNA delivery with nanoparticles bearing the optimal ligand.
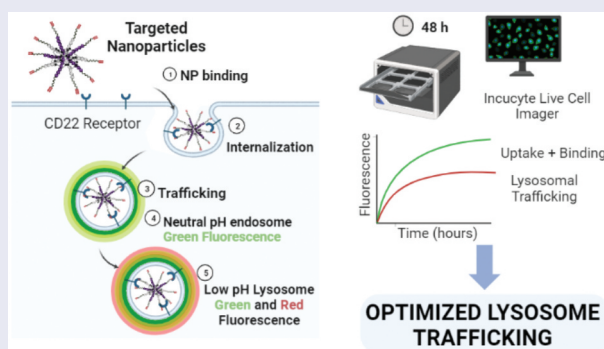
IMPACT STATEMENT

The ability of this pH-sensitive reporter platform to rapidly screen ligands in nanoparticle format will enable identification and production of targeted NPs with desired lysosome trafficking properties.

Introduction

Nanoparticles (NPs) are often considered for drug delivery applications due to their ability to tune drug physicochemical properties, protect drugs from degradation, and control drug biodistribution. NPs can be engineered to encapsulate a range of small molecule and large biologic payloads, such as nucleic acids, through covalent and non-covalent mechanisms [1]. In addition to optimizing physicochemical properties,

NPs may be functionalized with molecules designed to bind specific receptors expressed on target cells to improve selective delivery and uptake [2]. Targeting cell-surface receptors drives NP internalization by endocytosis which results in subcellular trafficking to endosomes and/or lysosome vesicles or recycling back to the cell surface depending on the receptor[3,4]. Endocytosis kinetics are dependent on the affinity of ligand-receptor interactions, internalization rate, and

---

ligand valency [3–5]. For therapeutic cargoes such as nucleic acids, NP delivery through receptor-mediated endocytosis is essential to gain cellular entry since these molecules are too large and polar to diffuse directly across cell membranes [6].

For macromolecular cargoes such as nucleic acids, cargo must be released into the cell cytoplasm for functional delivery [7]. The low pH (~5) of this subcellular compartment can be utilized to induce structural and/or physical changes in lysosome-targeted NPs to enable delivery of cargo into the cytosol [8,9]. To this end, many ionizable materials comprising functional groups with pKa ~ 5.5–6.5 have been developed to impart lysosome escape properties by triggering endosome swelling and destabilization of the lysosome membrane [10–12]. In order to exploit pH-responsive delivery mechanisms, NPs must be efficiently trafficked to lysosomes, and this trafficking is dependent on both ligand binding properties and receptor biology [13,14]. Therefore, to properly utilize receptor-mediated endocytosis and lysosomal trafficking pathways for NP delivery of nucleic acids, subcellular trafficking must be confirmed for a given ligand-receptor pair.

Current methods for observing lysosomal trafficking of NPs include co-incubation of fluorescent NPs with dyes that are sequestered in lysosomes (i.e. LysoTracker), evaluation in cell lines engineered to express fluorescent lysosome marker proteins such as green fluorescent protein (GFP)- LAMP1 fusions and collection of lysosomal extracts [15–18]. While these methods provide some insight into subcellular distribution of NPs, quantifying signals and modeling trafficking kinetics remain difficult. Co-localization experiments tend to be qualitative since not all lysosome compartments will contain NPs in a given cell at a given time, lysosome staining efficiency can vary, and retention of dyes within cells is influenced by efflux pumps [19]. Furthermore, not all NP formulations are amenable to dye-labeling due to the nature of the material, cargo, or both. Sophisticated optically active molecules have been developed for organelle-specific imaging [20–22], but these technologies are focused on gathering high resolution and dynamic information on specific organelle interactions and are not amenable to large, high throughput studies of NP uptake and lysosome trafficking for a variety of targeting ligand types.

To this end, we envisioned an NP platform capable of rapid ligand screening for both cell binding and lysosomal trafficking. This platform would screen ligands for their ability to bind and subsequently internalize and traffic to lysosome compartments, which is critical for NPs designed with pH-sensitive lysosome escape function to deliver therapeutics to the cytosol. The platform should be compatible with high-throughput live-cell imaging modalities to allow rapid evaluation of multiple ligands in multiple cell types. Furthermore, the platform should be drug- and cargo-agnostic and enable plug-and-play ligand functionalization.

Here, we report a cell binding and lysosome trafficking platform based on dual-labelled polyion complex (PIC) micelles [23,24]. Specifically, PIC micelles were formed by self-assembly of polyethylene glycol (PEG)-poly(glutamic acid) (PGA) and PEG-poly (L-lysine) (PLL) into nanostructures by electrostatic interaction, followed by covalent crosslinking. Block co-polymers were labelled with two fluorescent dyes to visualize NP binding and lysosome trafficking in live cells by fluorescence microscopy; a pH-insensitive dye (Alexa Fluor 488, AF488) and a pH-sensitive dye (pHrodo Red) that emits fluorescence only at low pH. In this configuration, association of green fluorescence with cells indicates binding and appearance of red fluorescence indicates lysosome trafficking. Finally, antibody fragment-based ligands were coupled to NPs through reaction of azides on PEG chains with non-natural amino acids in the ligands.

CD22 was selected as the cell surface receptor to validate the assay as it is a well-studied activator of receptor-mediated endocytosis and is of particular interest for pharmaceutical development of B cell therapeutics [25–28]. Ligands based on Pinatuzumab [29], Epratuzumab [30,31], and Moxetumomab [32,33] were attached to reporter NPs and uptake and lysosome trafficking was monitored by high throughput image analysis in AD-293 cells engineered to overexpress CD22 as well as B-cell cancer cells with endogenous CD22 receptor. The reporter platform demonstrated differences in lysosome trafficking efficiency between the ligand types, which correlated with differences in transfection efficiency of pH-sensitive NPs delivering DNA via the same anti-CD22 ligands. Our findings highlight the utility of identifying ligands that rapidly traffic to lysosomes for efficient nucleic acid delivery with pH-sensitive materials.

Experimental (methods and materials)

Polymer labeling

The following polymers were synthesized by Alamanda Polymers Inc. (Huntsville, AL): 50-unit poly(L)lysine with a 5 kDa azide terminated PEG (Az-PEG-PLL), 50-unit poly(L)glutamic acid with a 5 kDa methoxy terminated PEG (MeO-PEG-PGA). These reagents met quality control standards of the supplier, including identity by nuclear magnetic resonance (NMR) spectroscopy, PDI 1.00–1.20 by gel permeation chromatography (GPC), N_3-PEG-NH$_2$ molecular weight (MN) of 4500–5500, MN by NMR 11,900–14500, and DP$_n$ of PLKC and PGA block of 45–55. Polymers were reconstituted at 2 mg/mL PBS supplemented with 0.1 M

phosphate dibasic. Succinimidyl ester dyes were added to polymer solutions while stirring and reacted to 30 min. Alexa Fluor 488 succinimidyl ester (Thermo Fisher, Waltham, MA) was reacted with Az-PEG-PLL at a 0.6 dye:polymer ratio. This dye met the following quality control standards: absorption maximum 494 ± 3 nm, fluorescence maximum of 518 ± 4 nm, and purity >50% by HPLC. Phrodo Red succinimidyl ester (Thermo Fisher, Waltham, MA) was reacted with Az-PEG-PLL and MeO-PEG-PGA at a 4.8 and 1.1 dye: polymer ratio, respectively. This dye met the following quality control standards: absorption optical density 0.7 ± 0.07 at 561 ± 3 nm, fluorescence maximum of 585 ± 4 nm, and purity >70% by HPLC. Labeled polymers were dialyzed using 3.5 kDa Slide-A-Lyzer cassettes (ThermoFisher, Waltham, MA) against 100 mM NaCl for 1 day and water for 4 days at 4°C. Purified polymers were lyophilized and reconstituted at 5 mg/mL in 10 mM sodium phosphate (pH 7.2–7.4).

Molecular biology and construction of targeting ligands

General molecular biology techniques were conducted as previously described [34]. Antibody fragments (single chain Fv (scFv) and Fabs) directed against CD22 were designed based on the previously described antibody sequences of Moxetumomab (Lumoxiti) [35,36], Pinatuzumab [37,38], and Epratuzumab [38]. All genes were generated by gene synthesis. An scFv derived from Moxetumomab was constructed in a VH-VL orientation. A G_4S_1 linker was used as a spacer between VH and VL, and an amber codon was introduced in frame within this linker to designate the site for non-natural amino acid (nnAA) incorporation. In addition, a C-terminal $6 \times$ His tag was encoded to facilitate purification and quantitation. Fabs derived from Epratuzumab and Pinatuzumab were generated by gene synthesis. An amber stop codon was encoded in frame at position A114 of the CH1 region designating the site for nnAA incorporation. In each case, nnAA incorporation sites were selected to enable efficient conjugate formation and at sites distal to the antigen binding domains to minimize interference with antigen binding. All genes were cloned into a proprietary vector useful for stable expression in mammalian cells.

Cell culture and expression of scFvs and fabs containing CpHK [39]

All antibody constructs were cloned under control of the human CMV promoter in a vector that encodes the gene for glutamine synthase as a selectable marker. Antibody expressing stable pools were generated by transfection (MaxCyte, Inc. Rockville, MD) of CHO cells engineered to express the pylRS and tRNApyl as previously described [40]. The pylRS/tRNApyl pair enables efficient incorporation of nnAA in response to amber stop codons. Transfected cells were selected in CD CHO medium (Thermo Fisher Scientific, Waltham, MA) supplemented with methionine sulfoximine (Sigma-Aldrich, St. Louis, MO) in T175 flasks and grown at 37°C and 6% CO_2. Surviving pools were screened for antibody expression by fed-batch fermentations in 250-ml shake flasks in a shaking incubator (ATR Biotech, Worcester, MA) at 37°C in the presence of 6% CO_2, at 140 RPM and 80% relative humidity in the presence of 2 mM cyclopentadiene derivative (CpHK). Antibody titers for Fab were quantified by biolayer interferometry using anti-Human Fab-CH1 functionalized sensors (Pall ForteBio, Fremont, CA). Antibody titers for scFv were quantified by biolayer interferometry using anti-His functionalized sensors (Sartorius, Göttingen, Germany). The best producing pools were selected for scale-up and material generation using AstraZeneca proprietary production medium and feed regimens in the presence of 2 mM CpHK.

Ligand functionalization

To incorporate DBCO functionality for NP conjugation, each antibody fragment ligand was conjugated with a DBCO-PEG linker. Pina-Fab was functionalized with Bis-dPEG ®11-DBCO (Sigma-Aldrich, St. Louis, MO), and both Epra Fab and Moxe ScFv were functionalized with DBCO-dPEG ®12-MAL (Sigma-Aldrich, St. Louis, MO). PEG linkers met quality control standards set by the manufacturer: Bis-dPEG ®11-DBCO purity >98% and DBCO-dPEG ®12-MAL purity >97%. Ligands were prepared at 10% sodium phosphate (v/v). Linker was added at 20-fold molar excess to the ligand, and reaction was agitated at RT overnight. The product was dialyzed at 4°C for 2 days against 25 mM His, 150 mM NaCl using 3kDa MWCO Slide-A-Lyzer cassettes (ThermoFisher, Waltham, MA). Successful conjugation was confirmed by LC-MS analysis.

Liquid chromatography-mass spectrometry (LC-MS) analysis

Liquid chromatography-mass spectrometry analysis (LC-MS) was performed using an Agilent (Santa Clara, CA) 1260 series HPLC coupled with an Agilent 6520 Accurate-Mass Q-TOF LC/mass spectrometer. The high-performance liquid chromatography (HPLC) parameters, equipped with a reversed-phase (RP)-HPLC column (Zorbax 300 Diphenyl RRHD, 2.1×50 mm, 1.8 µm, Agilent #857750–944), were as follows: flow rate: 0.5 mL/min; elution method: a gradient of 90% A and 10% B up to 5.00 min and then 10% A and 90% B after 5 min; mobile phase A was HPLC-grade H_2O contained 0.1% (v/v) formic acid, and mobile phase B was acetonitrile contained

0.1% (v/v) formic acid. Mass spectrometry data were collected for a range of 100–3000 m/z, using positive ion mode, a gas temperature of 350°C, a nebulizer pressure of 48 psi, and a capillary voltage of 5,000 V. Mass spectrometry data were collected and processed using Agilent MassHunter Workstation Data Acquisition and MassHunter BioConfirm software (v.12.0, Agilent).

NP assembly and crosslinking

To form NPs, AF488-Az-PEG-PLL, Phrodo Red-Az-PEG-PLL, and Phrodo Red-MeO-PEG-PGA were combined at a ratio of 0.25:0.25:0.5 in 10 mM sodium phosphate (pH 7.2–7.4). The final total polymer concentration was 1 mg/mL. NPs assembled at room temperature for 10 min followed by size measurement using a Malvern ZetaSizer Ultra (Malvern, UK) and ZSXplorer software to confirm NP formation. Then, EDC (1-ethyl-3-(3-dimethylaminopropyl)carbodiimide hydrochloride) (ThermoFisher, Waltham, MA) was added at 10 molar excess of PEG-PGA polymer. The identity of EDC crosslinker was confirmed by ThermoFisher using ^{1}H NMR prior to batch release. NPs were rotated at room temperature to crosslink overnight and then dialyzed in 1X PBS for 3 days at 4°C using 100 kDa dialysis device (Repligen Corporation, Marlborough, MA) to completely remove EDC. NP concentration was determined by measuring the absorbance of AF488 dye using a Nanodrop 2000 (ThermoFisher, Waltham, MA) and a standard curve. To conjugate targeting ligands, DBCO-functionalized ligands were added to NPs at a 3.5-fold excess ligand to azide groups. NPs were rotated at RT overnight, then dialyzed in 1X PBS for 3 days at 4°C using 100 kDa Float-A-Lyzer dialysis device (Repligen Corporation, Marlborough, MA). Dialyzed NPs were filtered using a syringe filter with 0.2 μm pore size. NP concentration was determined by AF488 absorbance as previously described, and ligand conjugation efficiency was calculated by measuring the increase in A280 after ligand conjugation using a Nanodrop2000 spectrophotometer. Endotoxin levels in final tNPs were measured using Endosafe Compendial limulus amoebocyte lysate (LAL) Cartridges with 0.05 EU/ML sensitivity (Charles River, Wilmington, MA). tNPs were diluted 1:10,000 or 1:1,000,000 until within the detection range of the assay, then measured according to the manufacturer instructions.

NP pH titration

The pH of fluorescently labeled NPs was adjusted by diluting in sodium phosphate of pH 4.5, 5.5, 6.5, and 7.2. Fluorescence of NPs at varying pH was measured using a NanoDrop™ 3300 Fluorospectrometer (Thermo Fisher, Waltham, MA). Fluorescence

intensity was collected for both AF488 (Ex: blue LED, Em: 525 nm) and pHrodo Red (Ex: white LED, Em: 585) at fixed gain.

Cell culture

AD-293 cells were cultured in DMEM (Gibco, Billings, MT) supplemented with 10% Fetal Bovine Serum (Gibco, Billings, MT) and 1% Anti-Anti (Gibco, Billings, MT). AD-293 cells were engineered for stable expression of human CD22 protein with a puromycin resistance selection marker. AD-293 huCD22 + cells were maintained in DMEM (Gibco, Billings, MT) supplemented with 10% Fetal Bovine Serum (Gibco, Billings, MT), 1% Anti-Anti (Gibco, Billings, MT), and 2 μg/mL puromycin (Thermo Fisher, Waltham, MA). MV-4-11 cells were cultured in IMDM (Gibco, Billings, MT) supplemented with 10% Fetal Bovine Serum (Gibco, Billings, MT), and 1% Anti-Anti (Gibco, Billings, MT). OCI-Ly19 cells were cultured in MEM α (Gibco, Billings, MT) supplemented with 10% Fetal Bovine Serum (Gibco, Billings, MT), and 1% Anti-Anti (Gibco, Billings, MT). All cell cultures were maintained in a humidified incubator, at 37°C, with 5% CO_2.

CD22 expression profiling

Cell viability and concentrations were determined using an automated cell counter (Vi-Cell XR, Beckman Coulter, Brea, CA). Cells were spun and resuspended in complete culture medium to adjust cell concentration to 0.3×10^6 cells/mL and seeded into 96 well U-bottom plates. The Mouse IgG1 Kappa Isotype (Invitrogen 11-4714-81, Waltham, MA) and CD22 Monoclonal (Invitrogen 11-0229-42, Waltham, MA) antibodies were diluted according to protocol (0.1–5 ug/mL) in FACs buffer (PBS +1% BSA + 5% FBS + 0.1% sodium azide). The cells were incubated with the antibodies under standard conditions (37°C in humidified atmosphere containing 5% CO_2) for 30 min. After incubation cells were washed three times by centrifugation at 400 rpm for 3 min and resuspended in 100 μL of flow buffer (PBS + 2% FBS). Cells were then analyzed by BD LSRFortessa Cell Analyzer (BD Biosciences, Franklin Lakes, NJ) in FIT-C channel.

tNP in vitro uptake assay

tNPS were evaluated in AD-293 WT, AD-293 huCD22 +, MV411, and OCI-Ly19 cell lines. Prior to NP treatment, cells were seeded in tissue culture treated 96-well plates. AD-293 and AD-293 huCD22+ cells were seeded at 20,000 cells/well, and MV411, and OCI-Ly19

cells were seeded at 30,000 cells per well 24 h prior to treatment. Prior to treatment, cell media was exchanged for Opti-MEM™ (Gibco, Billings, MT), which resulted in improved image quality compared with culture media. NPs were added to cells at a 1 µg NP/well (1 ng/µL) in 96-well plates. After 4 h, NPs were removed, and growth media was replenished. Following tNP treatment, cells were imaged using an Incucyte® Live-Cell Analysis System (Sartorius, Göttingen, Germany). Images were analyzed using the Incucyte software.

To observe colocalization with lysosomes, cells were treated with 50 nM LysoTracker dye 1 h prior to treatment. To inhibit lysosome acidification, bafilomycin was added to cells at 500 nM concentration in cell culture media 24 h prior to NP treatment, then replaced with Opti-MEM™ (Gibco, Billings, MT) with 10% FBS immediately prior to treatment. To inhibit endocytosis, 5 mM sodium azide was added to cells 10 min prior to NP treatment.

Confocal imaging

Cells were seeded on glass bottom optical plates and treated with bafilomycin as described at 500 nM concentration 24 h prior to NP treatment. 30 min prior to imaging, nuclei were stained with Hoechst at 1:2500 dilution. At time $t = 0$ h, tNPs were added at a dose of 1 µg per well and imaged using a Nikon Ti2-E inverted microscope coupled to a Yokogawa W1 spinning disk confocal. Cells were maintained using a stage top Tokai Hit incubator chamber at 37°C and 5% CO_2 with humidity during imaging. Images were acquired using a 40× WI 1.15 NA objective. A Hamamatsu ORCA-FusionBT back-thinned sCMOS camera was used for capturing the spinning disk images. All images were taken with a 100-ms exposure time. With Z-stacks acquired using seven 0.4 µm steps for each image. The AF488 was acquired using a 488 nm laser for excitation with an ET525/36 m emission filter. The pHrodo Red was acquired using a 561 nm laser for excitation with a ET605/52 m emission filter. The Hoescht fluorescence was acquired using a 405 nm laser for excitation with a ET455/50 m, DAPI-ET emission filter. Images were acquired at 0, 2, and 4 h time points.

NP uptake by flow cytometry

Cells were treated with tNP for 4 h. Following tNP treatment, stained with Hoescht for 15 min at 1:2450 dilution in culture media. Following Hoescht treatment, cells were dissociated from culture plate using TrypLE (Gibco, Bilings, MT) for 5 min at 37C. After dissociation, cells were suspended in flow buffer (PBS +1% BSA + 5% FBS + 0.1% sodium azide). Flow cytometry was performed using a LSRFortessa™ Cell Analyzer (BD Biosciences, Franklin Lakes, NJ).

Free ligand labeling and uptake

All ligands were labeled with dye for free ligand uptake assays. Epra Fab and Moxe scFv were labeled with AF488 C5 Maleimide or pHrodo Red Maleimide (Thermo Fisher, Waltham, MA). 1.1 molar excess dye was added to ligand and allowed to react for 1 h at RT. Pina-Fab was labeled with NanoDrop™ sDIBO Alkyne Kits for AF488 or pHrodo Red (Thermo Fisher, Waltham, MA) following the manufacturer instructions and incubating overnight at RT. All labeled ligands were purified using Antibody Conjugate Purification Kit (Thermo Fisher, Waltham, MA) to remove free dye. Final ligand concentration and dye content were measured by Nanodrop 2000 (Thermo Fisher, Waltham, MA). Successful conjugation was confirmed by LC-MS analysis. To evaluate internalization, cells plated in 96 well plates were treated with equivalent ligand doses to 1 µg tNP treatment (0.96 µg/well scFv, 1.92 µg/well Fab). Cells were imaged using the Incucyte imager as previously described.

PLL DNA transfection

NPs were prepared with modified PEG-poly-L-lysine and DNA as previously described [41]. Briefly, PEG-PLL (PEG MW = 5000, PLL = 50 lysine units) was purchased from Alamanda Polymers, Inc. (Huntsville, AL). NHS-functionalized morpholino (MN) was custom-synthesized by SynChem Inc. (Elk Grove, IL). Modified PEG-PLL was prepared by reacting NHS-ester functionalized buffering groups with the lysine primary amines to form modified PEG-PLL-MN. PEG-PLL-MN was combined with plasmid DNA encoding for green fluorescent protein at a nitrogen to phosphate (N:P) ratio of 4. The PEG-PLL-MN was comprised of 50% azide-modified PEG-PLL (Az-PEG-PLL) and 50% methoxy modified PEG-PLL (MeO-PEG-PLL). DBCO-modified ligands were added to NPs in 1.25 molar excess and reacted overnight at RT. Conjugated NPs were added to cells at a DNA dose of 200 ng per well and incubated overnight. Cells were imaged for GFP expression using the Incucyte imager as previously described.

Data analysis and statistics

Data were analyzed and plotted using GraphPad Prism (v9) (San Diego, CA). Statistically significant differences between independent groups were determined by ordinary two-way ANOVA with Sidak's multiple comparisons. Significant differences are indicated by the following : *$p < 0.05$, **$p < 0.01$, ***$p < 0.001$, ****$p < 0.0001$.

Results and discussion

Internalization tracking nanoparticles (NPs) were designed and synthesized utilizing multiple chemistries/conjugation handles to enable dye-labelling, NP assembly, and ligand attachment as shown in Figure 1. NPs were formed by combining two oppositely charged block co-polymers: cationic 50-unit poly(L) lysine with a 5 kDa PEG (PEG-PLL) and anionic 50-unit poly(L)glutamic acid with a 5 kDa PEG (PEG-PGA) Figure 2(a). PEG-PLL and PEG-PGA were combined at a 1:1 molar ratio and allowed to self-assemble by charge interactions to form polyion complex (PIC)
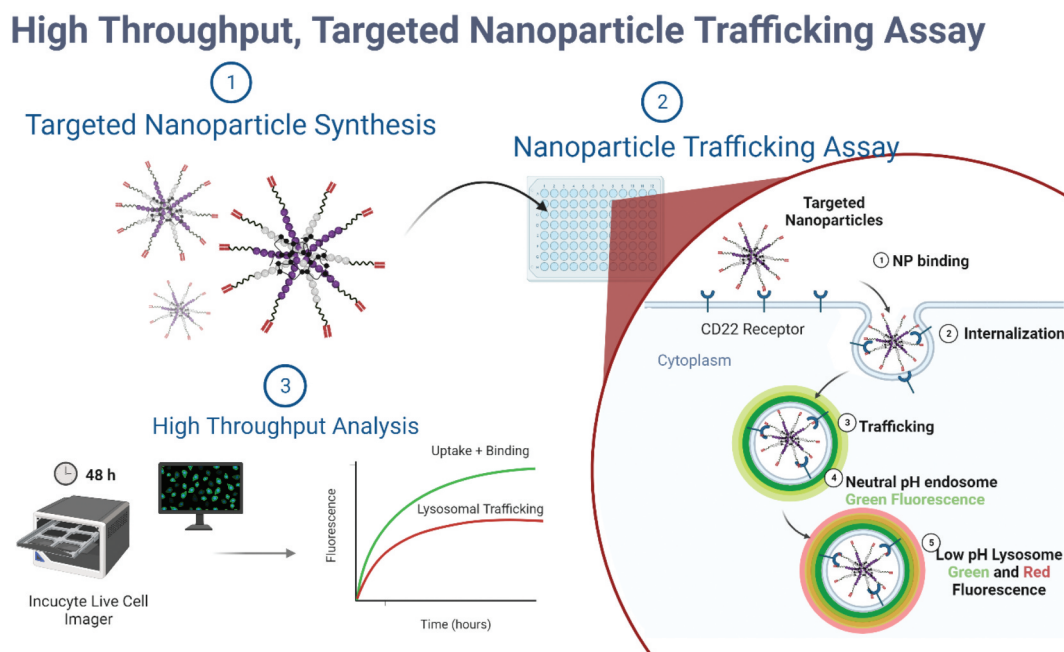

Figure 1. Schematic outlining procedure for evaluating targeting ligands using high throughput internalization assay. Created with BioRender.com.
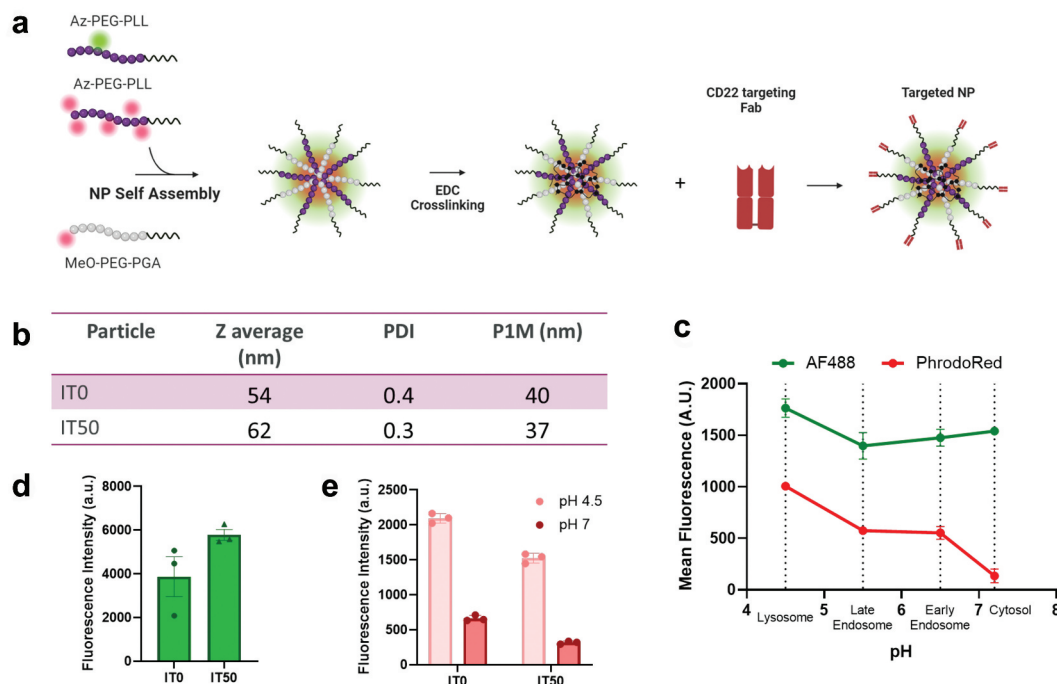

Figure 2. NP synthesis and characterization. (a) Synthesis scheme for tNP created with BioRender.com. (b) Size and polydispersity of non-functionalized NPs (IT0) and 50% azide functionalized NPs (IT50) by dynamic light scattering (DLS). PDI = polydispersity index, P1M = peak one mean size (c) tNP fluorescence in green (AF488) and red (pHrodo red) channels under varying physiological pH conditions. (d) Fluorescence intensity of IT0 and IT50 NPs in AF488 channel at pH 7. (e) Red fluorescence intensity of IT0 and IT50 NPs in pHrodo red channel at pH 4.5 and pH 7. Data is represented as the average ± SEM of $N = 3$ nanoparticle preparations.

micelles. Amines in these polymers served as dye-attachment points to install fluorescent reporters (discussed below). To improve NP stability, EDC was added at 10 molar excess to cross-link amines in PEG-PLL side chains with carboxyl groups in PEG-PGA side chains. Finally, antibody-based ligands were conjugated to the NP surface to create a targeted NP. The resulting NPs were 50–60 nm in diameter with a polydispersity index (PDI) of 0.3–0.4 Figure 2(b).

Polymers were labeled with fluorophores prior to NP assembly to enable visualization of uptake and lysosomal trafficking. Alexa Fluor 488 (AF488) emits green fluorescence with no pH responsiveness, allowing for visualization of total NP binding and uptake. pHrodo Red emits red fluorescence under acidic conditions, allowing for specific visualization of NPs trafficked to lysosomes [42]. Polymers were labeled by conjugating NHS ester dyes to lysine amine residues and/or the N-terminal amine on the polymer (PEG-PLL) or the N-terminal amine only (PEG-PGA). PEG-PLL was modified with AF488 NHS at a target ratio of 0.6 dyes per polymer and PEG-PLL and PEG-PGA were both modified with pHrodo Red NHS ester at a target ratio of 4.8 and 1.1 dyes per polymer, respectively. Using an estimated association number of 10 polymers per NP [43], the dye content of NPs comprised of these polymers was 1.5 AF488 and 17 pHrodo Red dye molecules per NP. pHrodo Red was incorporated at a ~ 11X higher ratio than AF488 due to the low quantum yield of pHrodo Red, even at low pH [44]. pHrodo Red content required optimization, as initial constructs prepared with low levels of dye being too dim to visualize in cells, which led to increasing dye labelling of PEG-PLL and also labelling PEG-PGA with pHrodo Red NHS. To understand potential quenching effects of high density pHrodo Red labeling, PEG-PLL polymer was labeled with dye:polymer ratios from 0.6–4.8. Fluorescence increased linearly with increasing dye content, and no quenching was observed within this range (Supplementary Figure S1). Excessive dye labeling decreased NP stability and impacted ligand conjugations, which should be considered if further optimization is desired.

Resulting dye-labeled NPs showed pH-independent AF488 fluorescence over physiologically relevant pH conditions, while pHrodo Red fluorescence increased in low pH conditions (Figure 2c). The mean fluorescence intensity of pHrodo Red was ~ 7.5X higher at lysosomal pH 4.5 than at pH 7.2 in simple buffer solutions, demonstrating the desired pH-response of reporter NPs. Fluorescence intensity of AF488 varied less than 20% over the same range. AF488 signal is independent of pH and is expected to be similar for NPs which are membrane-bound, sequestered in

intracellular compartments, or localized to the cytosol. However, pHrodo Red fluorescence is highly pH-dependent, and signal intensity corresponds with lysosomal trafficking. Therefore, by measuring both AF488 and pHrodo Red signal, NP uptake and lysosome trafficking may be tracked independently.

NP functionalization with targeting ligands occurred through azide-modified PEG polymers incorporated into the NP assembly mixture, enabling conjugation with DBCO-ligands post NP formation. Targeting ligand density was controlled by the stoichiometry of reactive azide-PEG and inert methoxy-PEG polymers used to form NPs. NPs formulated with 0% azide-PEG polymer are termed IT0, and NPs formulated with 50% azide-PEG polymer are termed IT50. These two NP formulations do not have significantly different fluorescence profiles in the green and red channels corresponding to AF488 and pHrodo Red fluorescence, and pH sensitivity of pHrodo Red was confirmed in both IT0 and IT50 Figure 2(d,e). This allows for direct comparison between targeted (IT50) and non-targeted (IT0) NPs to assess the effect of targeting on uptake and lysosomal trafficking.

Following formulation and initial characterization, the NP platform was employed to evaluate antibody-based ligands targeting CD22, a commonly overexpressed receptor in B cell lymphoma with demonstrated efficacy as a binding site for immunoconjugates and targeted liposomes [25,45]. This target was selected because CD22 is a well-characterized endocytic receptor with demonstrated ability to traffic bound ligands to intracellular compartments [27,46]. CD22 is a recycling receptor, and ligand properties including binding affinity, pH responsiveness, and specific binding epitope have been shown to influence intracellular trafficking and recycling of antibody conjugates [38,47]. Three antibody-based CD22-binding ligands were selected for assessment as NP targeting agents: antibody fragments (Fab) derived from pinatuzumab (Pina Fab) and epratuzumab (Epra Fab), and a single-chain variable fragment (scFv) derived from moxetumomab (Moxe scFv). These molecules are developed from monoclonal antibodies against CD22 that have progressed into the clinic for the treatment of leukemia and/or lymphoma [29,48–53]. These three molecules all bind CD22 with approximately single-digit nM dissociation constants, have been shown to bind different epitopes on CD22 [38] and incorporate different protein engineering strategies [54] (Supplementary Table S1) [36,55–57].

CD22-binding ligands were conjugated to NPs using azide-DBCO ligation. Ligands were expressed containing non-natural amino acids (nnAAs) incorporated at position A114 (Kabat numbering) for Pina- and Epra-Fabs, with alanine mutated to nnAA. Moxe scFv comprised nnAA incorporated at the linker between the VH

and VL domains. Reactive chemistry of nnAAs included cyclopentadiene-derivative CpHK [58] (Epra-Fab and Moxe-scFv) and azide (Pina-Fab) appended to the lysine side chains (Figure 3a) and expressed using a modified pyrrolysine expression system in CHO cells [34,39]. All ligands were conjugated with PEG linkers to incorporate DBCO functionality to enable reaction with azide-functionalized NPs, as shown in Figure 3b. A hetero-bifunctional PEG(11) linker with maleimide and DBCO chemistries were conjugated to molecules with cyclopentadiene functionality (Epra Fab, Moxe ScFv), and bis-DBCO PEG(11) linker was conjugated to molecules with azide functionality (Pina Fab). Successful conjugation was confirmed by mass spectrometry (MS) with nearly quantitative conversion (Supplementary Table S2). Increases in molecular weight post-conjugation correspond to the size of the DBCO linker (Figure 3c,d, Supplementary Figure S2). Following DBCO functionalization, CD22 targeting ligands were conjugated to NPs via copper-free azide-alkyne [2 + 3] cycloaddition 'click' chemistry [59]. IT50 NPs were incubated overnight at room temperature (RT) with 3.5-fold excess of DBCO-ligand relative to azide groups, then purified by dialysis to remove unconjugated ligand. Conjugation efficiency was 40–70%, resulting in 2–4 targeting ligands per NP on average determined by measuring UV absorbance at 280 nm

before and after ligand conjugation (Figure 3b). Resulting targeted NPs (tNPs) showed an increase in the primary peak from 40 nm to 60–90 nm by dynamic light scattering (DLS) following ligand conjugation (Supplementary Table S3, Supplementary Figure S3). Endotoxin levels of tNPs were below the limit of detection by limulus amoebocyte lysate (LAL) assay.

Given the reported similarities of these CD22-binding ligands, we sought to employ the internalization reporter NP system to determine their behavior as ligands for NP delivery, and if differences exist, whether they impact functional outcomes of drug delivery systems. To evaluate target-specific internalization, CD22-negative AD-293 cells were engineered to overexpress human CD22. CD22 over-expression relative to wild-type (WT) parental AD-293 cells was confirmed by flow cytometry using a commercially available anti-CD22 antibody (Supplementary Figure S4). To visualize cell internalization properties of free ligand, Pina-Fab, Epra-Fab, and Moxe-scFv were fluorescently labeled with AF488 and pHrodo dyes through site-specific conjugation to the same nnAA handles used for NP attachment in later studies, with successful conjugation of 1 dye per ligand confirmed by liquid chromatography–mass spectrometry (LC–MS) (Supplementary Figure S5, Supplementary Table S4). Wild-type (WT) CD22-negative and CD22 overexpressing (CD22+) AD-293 cells were incubated with fluorescently tagged ligands, and fluorescence was
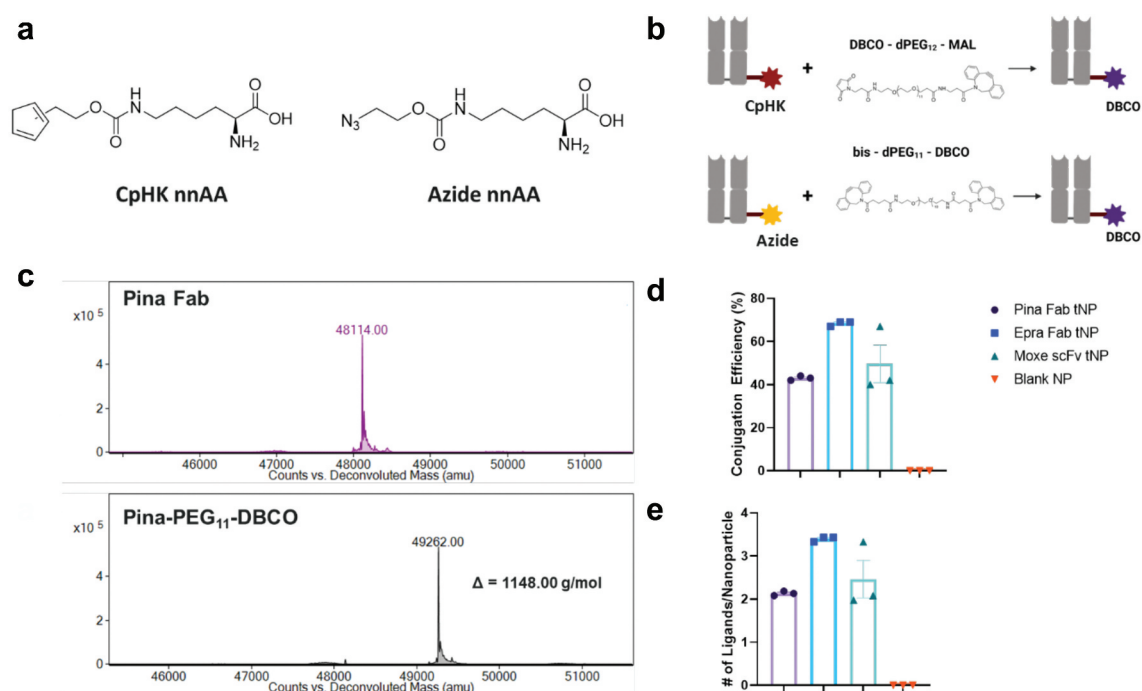

Figure 3. Targeting ligand preparation and conjugation (a) structures of nnAAs with reactive cyclopentadiene or azide chemistries appended to lysine side chains (b) modification of CpHK- and lysine azide-tagged targeting ligands with DBCO-PEG linker (c) Representative LC-MS of Pina Fab before and after functionalization with DBCO PEG linker. The resulting mass shift of 1148 g/mol corresponds to the molecular weight of the linker. (d) Conjugation efficiency of DBCO-functionalized ligands to IT50 NPs and (e) calculated average number of ligands per NP measured by UV absorbance at 280 nm. Data is represented as the average ± SEM of $N = 3$ nanoparticle preparations.

quantified over time (Supplementary Figure S6). All ligands showed similar levels of AF488 signal, with fluorescence increasing steadily over 2–3 h before reaching a plateau. pHrodo red signal differed between the ligands, with Pina-Fab showing 12- and 5-fold higher signal than Epra Fab and Moxe scFv respectively. This suggests that Pina-Fab is trafficked more efficiently to lysosomes than Epra Fab and Moxe scFv. AF488 and pHrodo Red fluorescence was reduced in WT cells compared with CD22+ cells, indicating that these ligands interact specifically with the CD22 receptor with minimal non-specific interaction. It is important to note that these results highlight binding and internalization of monovalent ligands and behavior could change with increased valency in antibody (bivalent) or nanoparticle (multivalent) formats. Additionally, ligands were not bright enough to be evaluated in the live-cell imaging assay (discussed below).

With tNPs in hand, the high-throughput cell-based component of the assay was established. To evaluate target-specific internalization, WT and CD22+ AD-293 cells were seeded in 96-well plates, then incubated with 10 ng/μL IT50 tNPs with Pina Fab, Epra Fab, or Moxe scFv targeting ligands. Cells were treated for 4 h, then NPs were removed and replaced with fresh media. Non-targeted IT0 NPs were used as a control to test for non-specific interactions. Following the addition of NPs, cellular fluorescence was measured over time by high content imaging using an Incucyte system, which enables high-throughput live fluorescence imaging of cells in multi-well plates. Images were acquired at 30 or 60 min intervals for up for 60 h. Fluorescence intensity in resulting images was analyzed using the Incucyte image analysis software. Thresholds were generated to identify fluorescence signal above background (untreated cells), and fluorescence was reported as Total Integrated Intensity (CU x μm²/Image), which is the total sum of the masked objects' fluorescence intensity in each image. This general assay design was adapted for subsequent studies with slight variations depending on the intended read-out.

Next, mechanistic studies were performed to validate the assay's ability to accurately report cell uptake and subcellular trafficking. Active uptake of tNPs by receptor-mediated endocytosis was confirmed by pre-treating CD22+ cells with sodium azide, a metabolic inhibitor which blocks ATP-dependent uptake pathways including receptor-mediated endocytosis [60]. Sodium azide treatment resulted in significant reduction in both AF488 and pHrodo Red signal compared with cells treated with tNPs alone (Figure 4a,b). While AF488 signal was reduced, it was not eliminated, likely attributed to cell surface binding by tNPs which is not expected to be affected by sodium azide treatment. pHrodo Red signal was nearly undetectable under the same conditions, confirming that without endocytosis pHrodo Red signal is not produced.

Localization of pHrodo-Red signal within acidic lysosomal compartments was confirmed by pretreating cells with the lysosome pH neutralizer bafilomycin (BA1), which blocks both endosome acidification by H±ATPase inhibition and lysosome fusion [61]. AF488 signal indicated continued cellular uptake of Pina Fab tNPs in BA1-treated cells; however, pHrodo Red signal was completely abolished (Figure 4c–e). This result indicates that pHrodo Red signal is dependent on tNP trafficking to low pH lysosomes.
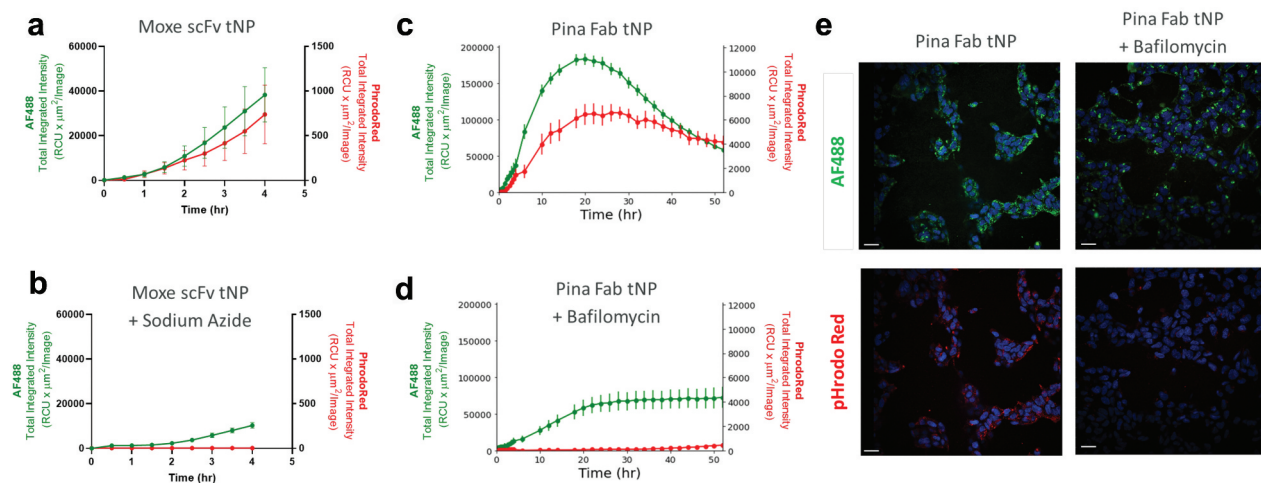

Figure 4. Uptake and trafficking response to endocytosis inhibitors internalization assay was performed using Moxe-scFv tNPs in untreated CD22+ AD-293 cells (a) or cells pretreated with 5 mM sodium azide (b). Similarly, the assay was repeated using Pina Fab tNPs in untreated CD22+ AD-293 cells (c) or cells pretreated with bafilomycin (d). Confocal imaging of cellular uptake of Pina Fab tNPs is shown in (e). Scale bar = 30 nm. Blue = Hoescht nuclear stain, green = AF488 fluorophore, red = pHrodo red fluorophore. All data is represented as the average ± SEM of N = 3 biological replicates.

To further correlate pHrodo Red signal with lysosome trafficking, co-staining with LysoTracker dye was used as an orthogonal method. LysoTracker probes are comprised of a fluorophore and a weak base. The probes freely diffuse across membranes at neutral pH, but become charged in acidic environments leading to accumulation of dye in lysosomes [62,63]. Cells were treated with LysoTracker and Pina Fab tNPs, imaged for lysosomal staining and NP fluorescence over time, and analyzed for colocalization of the fluorescent signals by Pearsons correlation coefficient calculations (Supplementary Figure S7, Supplementary Figure S8). The Pearson's coefficient of tNP AF488 signal with LysoTracker increased over time, indicating trafficking of NPs to lysosomes. Colocalization was higher in CD22+ cells compared with WT cells, indicating that lysosomal trafficking is more efficient following receptor-mediated endocytosis than non-targeted uptake pathways. The Pearson's coefficient of tNP pHrodo Red signal with LysoTracker increased linearly over time, correlating lysosomal trafficking with increased pHrodo Red fluorescence.

Following validation that cell binding and internalization of reporter NPs could be observed and quantified, this assay was employed to compare internalization and trafficking of tNPs bearing Pina Fab, Epra Fab, Moxe scFv in WT and huCD22+ AD-293 cells. Cells were incubated with tNPs or non-targeted IT0 NPs as a control. Uptake of tNPs and non-targeted NPs were measured by tracking fluorescence of AF488 and pHrodo Red by high content imaging (Figure 5a–d). Fluorescence intensity of both fluorophores increased over time, as NPs were taken up by target cells. CD22-targeted uptake was highest for Pina tNP based on AF488 signal, followed by scFv tNP, while lysosomal trafficking was enhanced for Pina tNP compared with all other treatments based on pHrodo Red signal. Overall, Pina tNPs showed the best overall combination of targeted uptake and lysosomal trafficking in CD22+ AD-293 cells and low non-specific uptake in CD22 negative WT cells. Epra tNPs showed lower targeted uptake in CD22+ cells and also minimal non-specific uptake in WT cells. scFv tNPS and blank IT0 NPs showed high uptake and trafficking in both target CD22+ and non-target WT cells. Significant uptake of non-targeted NPs was observed, which can be attributed to non-specific uptake pathways such as macropinocytosis, which may have different lysosome trafficking properties than receptor-
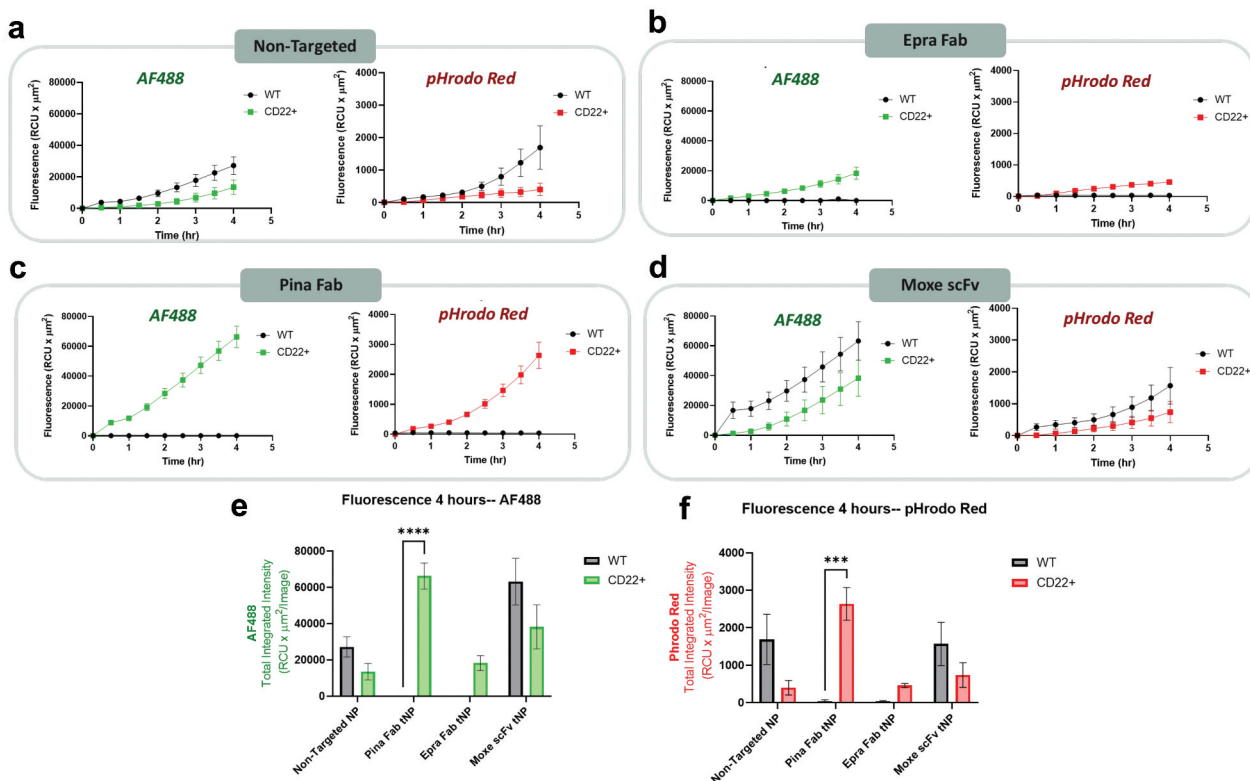

Figure 5. CD22-targeted internalization of tNPs in engineered CD22 + AD-293 cells. (a-d) fluorescence intensity of AF488 and pHrodo Red following treatment with non-targeted and CD-22 targeted NPs at a dose of 1 μg/well. Imaging and analysis were performed using the incucyte high content imager. Peak fluorescence intensity for each tNP formulation in the AF488 (e) and pHrodo Red (f) channels are shown. Comparisons between fluorescence of WT and CD22 + cells were performed using two-way ANOVA with Sidak multiple comparisons test. ***$P < 0.001$, ****$P < 0.0001$. All data are represented as the average ± SEM of $N = 3$ biological replicates.

specific endocytosis via CD22. This non-specific uptake is most evident in non-engineered CD22 negative WT AD-293 cells. Overall, Pina tNP shows optimal uptake efficiency and target specificity in engineered AD-293 cells (Figure 5e–f). Further, when data were plotted as a ratio of pHrodo Red signal to AF488 signal, Pina Fab tNPs showed significant ratios than non-targeted NPs or other tNPs. This indicates that Pina Fab tNPs traffic to lysosomes more efficiently in AD293 cells engineered to express CD22, independent of uptake rate (Supplementary Figure S9).

Uptake studies were repeated for all tNPs in relevant cancer cell lines. OCI-Ly19 is a diffuse large B cell lymphoma cell line that expresses CD22 at a physiologically relevant level, which is significantly lower than expression levels in engineered CD22+ AD-293 cells. MV411 is an acute myeloid leukemia cell line that does not express CD22, serving as a negative control. CD22 expression levels on all cell lines were confirmed by flow cytometry (Supplementary Figure S2). In OCI-Ly19 cells, Pina Fab and Moxe scFv tNPs show the highest amount of uptake and lysosomal trafficking, while uptake of Epra Fab tNPs was significantly lower (Figure 6a,b). All tNPs showed no off-target uptake in CD22- MV411 cells. Furthermore, all tNPs showed enhanced on-target uptake in OCI-Ly19 compared with blank IT0 NPs, which showed low levels of uptake and lysosomal trafficking in both OCI-Ly19 and MV411 cells. AF488 and pHrodo Red signal increase

linearly for 20 h, before reaching a plateau (Figure 6c–f). Taken together, these results indicate that CD22 targeting ligands facilitate enhanced uptake and lysosomal trafficking in CD22+ B cell lymphoma cell lines, with Pina Fab and Moxe scFv showing the highest uptake and lysosome trafficking.

The utility of this assay relies on the ability to identify ligands for optimal lysosome trafficking of tNPs, which should also enhance the function of nanocarrier systems that utilize low pH-related mechanisms for delivery. To confirm translatability of the cell trafficking assay, pH-sensitive tNPs delivering DNA were evaluated to determine if the optimal ligand identified in the reporter format corresponded to the best ligand for functional nucleic acid delivery. Gene delivery tNPS were constructed with PEG-poly-(L Lysine) (PLL) bearing pH-sensitive morpholino groups were prepared with GFP DNA cargo as previously described [41] and conjugated with Pina Fab, Epra, Fab, and Moxe scFv using DBCO-azide chemistry. Two PEG-PLL polymers were used: one with a terminal methoxy group (MeO-PEG-PLL) and another incorporating azide chemistry (N_3-PEG-PLL), serving as a reactive handle for ligand conjugation. MeO-PEG-PLL and N_3-PEG-PLL were mixed at a 1:1 ratio to target a final surface ligand density of 50%. The PEG-PLL mixture was combined with plasmid DNA at an nitrogen to phosphate (N:P) ratio of 4 in aqueous buffer and incubated at RT for 10 min to allow NP formation by electrostatic
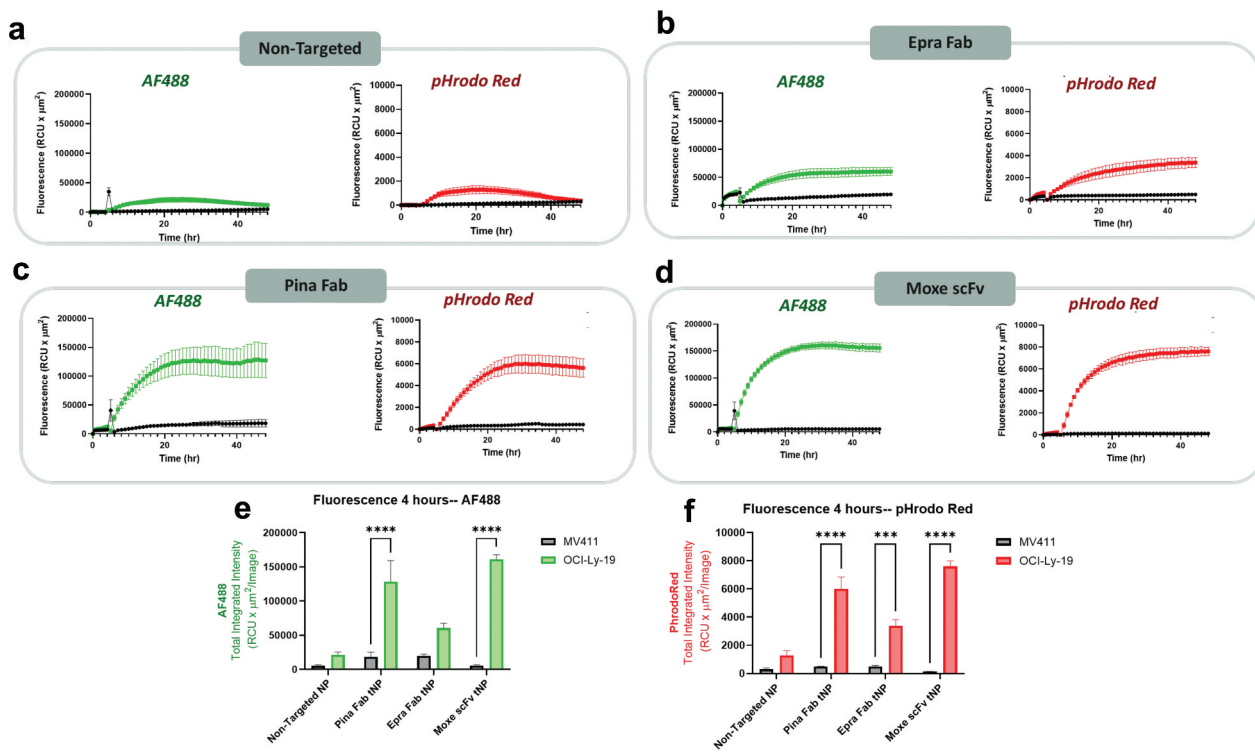

Figure 6. CD22-targeted internalization of tNPs in cancer cell lines MV411 and OCI-Ly-19. (a-d) fluorescence intensity of AF488 and pHrodo red in MV411 (CD22-) and OCI-LY-19 (CD22+) following treatment with non-targeted and CD22 targeted NPs at a dose of 1 µg/well. Imaging and analysis were performed using the incucyte high content imager. Peak fluorescence intensity for each tNP formulation in the AF488 (e) and pHrodo red (f) channels are shown. Comparisons between fluorescence of MV411 and OCI-Ly-19 cells were performed using two-way ANOVA with Sidak multiple comparisons test. ***$P < 0.001$, ****$P < 0.0001$. All data are represented as the average ± SEM of $N = 3$ biological replicates.

complexation. Targeting ligands were added to the NP solution at 1.25-fold excess to azide groups, and the conjugation reaction proceeded overnight. The resulting gene delivery tNPs were similar in size to non-targeted NPs, with no significant difference in NP properties with different targeting ligands (Figure 7a, Supplementary Table S5).

WT and CD22+ AD-293 cells were transfected with PLL tNPs, and GFP expression was monitored over time (Supplementary Figure S10). Amongst the tNPs tested only PLL NPs targeted with Pina Fab showed significantly enhanced transfection in CD22+ over WT AD-293 cells (Figure 7b,c). Non-targeted NPs, Epra Fab, and Moxe scFv targeted PLL tNPs all showed similar transfection rates in WT and CD22+ cells, indicating significant non-specific interactions and/or a high endocytic rate for this cell line independent of targeting. This result is consistent with results of the reporter assay in AD-293 cells, which also indicated non-specific uptake of non-targeted NPs in this cell type. Further, Pina-Fab-targeted PLL NPs showed the highest GFP expression in CD22+ cells of all NP formulations. This result correlates with Pina-Fab tNP uptake and lysosomal trafficking in CD22+ AD-293 cells, indicating that this assay has the potential to identify ligands with optimal properties for targeted delivery of nucleic acids where low pH is required for functional delivery.

In summary, we describe a high-throughput, plug-and-play assay to enable direct screening of targeting ligands in NP format. This assay captures cell binding and lysosome trafficking of targeted NPs, allowing for quantitative evaluation of internalization, subcellular trafficking, and the kinetics of these properties. In the case of CD22-targeting, the assay platform was able to discern differences amongst three known antibody-based ligands, which aligned with differences in functional delivery of DNA with targeted NPs. The fact that all CD22 ligands were not equally effective for targeted nano-delivery highlights the importance and opportunity to confirm trafficking properties to maximize effectiveness of targeted delivery.

While this assay has demonstrated utility, it also has limitations. NP preparation is the greatest source of variability for this assay. Potential sources of variation include dye conjugation efficiency, degree of cross-linking, NP size, reactive group content, and ligand conjugation efficiency. Therefore, it is recommended to use the same batch of NPs within experiments to reduce variability and allow for comparison between NPs. It is also important to establish consistent quality control requirements to ensure that different tNPs have similar size, fluorescence, and protein content. To improve consistency of downstream analysis, image analysis protocols were established using the Incucyte and were automated to eliminate bias or variability between users.

This assay was developed as a cargo-agnostic reporter system for quantitative evaluation of lysosome
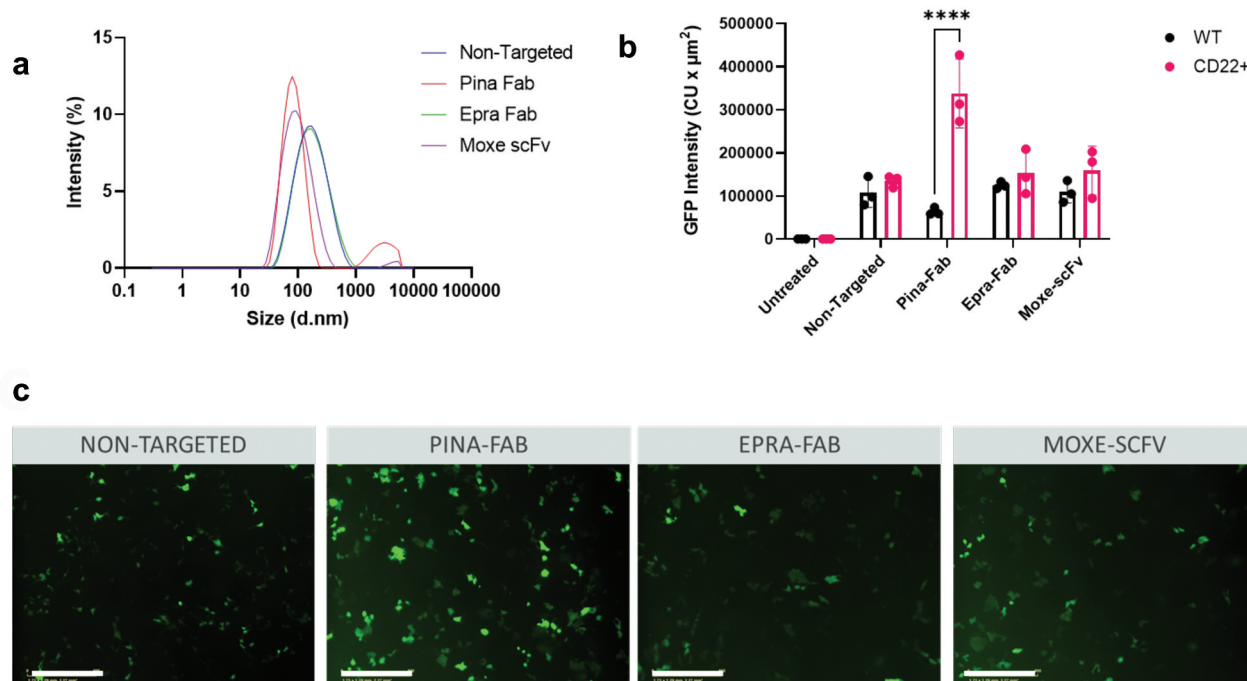

Figure 7. Performance of CD22 targeting ligands for GFP DNA delivery using PLL-based NPs. (a) Size of non-targeted and CD22-targeted NPs by DLS. (b) GFP expression by image analysis of WT and CD22+ AD-293 cells 62 h after transfection with PLL NPs. Comparisons between GFP expression of MV411 and OCI-Ly-19 cells were performed using two-way ANOVA with Sidak multiple comparisons test. ****$p < 0.0001$. All data are represented as the average ± SEM of $N = 3$ biological replicates. (c) Images of GFP expression in CD22+ AD-293 cells 62 h after transfection. Scale bar = 400 μm.

trafficking. While advanced molecular probes have been developed and described for advanced imaging of various organelles [20–22], this assay was specifically designed to track targeted NP trafficking to lysosomes. Lysosome trafficking and endosomal escape have been identified as major bottlenecks for productive intracellular delivery, so it is important to specifically interrogate this process. Future iterations of this platform may include additional reporters to clarify biological processes and subcellular mechanisms.

Further, it is important to note that this assay is only relevant to understand NPs with similar physiochemical properties to this platform. For example, cationic NPs will interact nonspecifically with cell membranes by charge interactions, and this interaction may dominate over targeting ligand interactions with the target receptor. Additionally, using NPs with dramatically different shape and size, such as nano rods or filamentous NPs, would affect interactions between the particle and cell surface. Therefore, tNP properties should be well-matched to the particles of interest in order to accurately predict intracellular delivery properties.

Selecting optimal targeting ligands through understanding subcellular processes associated with productive delivery will enable improved design of nano-delivery systems. Further refinement of drug delivery systems to dial-in subcellular function could be critical to realize next-generation systems with improved therapeutic index [64,65]. Furthermore, the basic assay design described here could be further expanded-on to answer more complex questions regarding trafficking and function of targeted NPs and further guide NP design. As such, several reporter systems have been described recently that can detect lysosome rupture, autophagy, and nuclear delivery, demonstrating the need and value for subcellular diagnostic agents [66–69].

Conclusion

Targeted NPs hold promise for enabling targeted delivery of biological cargoes with a high degree of specificity. While targets have been identified for a wide range of disease indications, it is difficult to predict the efficacy of targeting ligands for productive intracellular delivery. Subcellular localization is impacted by properties of the target, including rate of endocytosis, rate of recycling, abundance and localization on the cell surface. Internalization is also impacted by properties of the targeting ligand, including binding affinity and epitope, pH responsiveness, and valency. All too often a 'one-size fits all' approach is employed in targeted NP production, assuming that antigen binding alone is sufficient to achieve the maximum desired benefit. The assay reported here captures internalization and lysosome trafficking

properties of targeted NPs, allowing for quantitative evaluation of internalization, lysosome trafficking, and the kinetics of these events. Thus, targeted NPs can be optimized to select the best targeting ligand for applications requiring lysosome trafficking.

Using CD22 targeting ligands as a proof of concept, we found that the ligand with the highest lysosome trafficking determined by the NP reporter assay was Pina Fab, which subsequently also showed the highest efficacy for targeted DNA delivery. Parameters such as ligand density could be further tuned using this platform by varying the density of reactive handles on the NP to find the optimal density for a particular target. Altogether, the ability of this reporter platform to rapidly screen ligands in nanoparticle format, and the plug-and-play design of the pH-sensitive reporter NP will enable identification and production of targeted NPs with desired lysosome trafficking properties.

Disclosure statement

All authors are past or current employees of AstraZeneca.

References

[1] Afzal O, Altamimi ASA, Nadeem MS, et al. Nanoparticles in drug delivery: from history to therapeutic applications. Nanomaterials (Basel). 2022;12(24):4494. doi: 10.3390/nano12244494

[2] Mitchell MJ, Billingsley MM, Haley RM, et al. Engineering precision nanoparticles for drug delivery. Nat Rev Drug Discov. 2021;20(2):101–124. doi: 10.1038/s41573-020-0090-8

[3] Åberg C. Kinetics of nanoparticle uptake into and distribution in human cells. Nanoscale Adv. 2021;3 (8):2196–2212. doi: 10.1039/D0NA00716A

[4] Hoare SRJ. Analyzing Kinetic Binding Data. In: Markossian S, Grossman A, Arkin M, et al., editors. Assay Guidance Manual [Internet]. Bethesda (MD): Eli Lilly & Company and the National Center for Advancing Translational Sciences; 2004.

[5] Cao J, Zhang Y, Wu Y, et al. The effects of ligand valency and density on the targeting ability of multivalent nanoparticles based on negatively charged chitosan nanoparticles. Colloids Surf B Biointerfaces. 2018;161:508–518. doi: 10.1016/j.colsurfb.2017.11.015

[6] Manzanares D, Ceña V. Endocytosis: The Nanoparticle and Submicron Nanocompounds Gateway into the Cell. Pharmaceutics. 2020; 12(4):371. doi: 10.3390/pharmaceutics12040371

[7] Mendes BB, Conniot J, Avital A, et al. Nanodelivery of nucleic acids. Nat Rev Meth Primers. 2022;2(1):1–21. doi: 10.1038/s43586-022-00104-y

[8] Misinzo G, Delputte PL, Nauwynck HJ. Inhibition of endosome-lysosome system acidification enhances porcine circovirus 2 infection of porcine epithelial cells. J Virol. 2008;82(3):1128. doi: 10.1128/JVI.01229-07

[9] Chen P, Yang W, Hong T, et al. Nanocarriers escaping from hyperacidified endo/lysosomes in cancer cells allow tumor-targeted intracellular delivery of antibodies to therapeutically inhibit c-MYC. Biomaterials. 2022;288:121748. doi: 10.1016/j.biomaterials.2022.121748

[10] Urello M, Hsu W-H, Christie RJ. Peptides as a material platform for gene delivery: emerging concepts and converging technologies. Acta Biomaterialia. 2020;117:40–59. doi: 10.1016/j.actbio.2020.09.027

[11] Sharma A, Vaghasiya K, Ray E, et al. Lysosomal targeting strategies for design and delivery of bioactive for therapeutic interventions. J Drug Targeting. 2018;26(3):208–221. doi: 10.1080/1061186X.2017.1374390

[12] Rathore B, Sunwoo K, Jangili P, et al. Nanomaterial designing strategies related to cell lysosome and their biomedical applications: a review. Biomaterials. 2019;211:25–47. doi: 10.1016/j.biomaterials.2019.05.002

[13] Ritchie M, Tchistiakova L, Scott N. Implications of receptor-mediated endocytosis and intracellular trafficking dynamics in the development of antibody drug conjugates. MAbs. 2013;5(1):13–21. doi: 10.4161/mabs.22854

[14] Devanaboyina SC, Lynch SM, Ober RJ, et al. The effect of pH dependence of antibody-antigen interactions on subcellular trafficking dynamics. MAbs. 2013;5(6):851–859. doi: 10.4161/mabs.26389

[15] Albrecht LV, Tejeda-Muñoz N, De Robertis EM. Protocol for probing regulated lysosomal activity and function in living cells. STAR protoc. 2020;1(3):100132. doi: 10.1016/j.xpro.2020.100132

[16] Barral DC, Staiano L, GuimasAlmeida C, et al. Soldati C and Seabra M C 2022 current methods to analyze lysosome morphology, positioning, motility and function. Traffic. 2022;23(5):238–269. doi: 10.1111/tra.12839

[17] Duan X, Tong Q, Fu C, et al. Lysosome-targeted fluorescent probes: design mechanism and biological applications. Bioorg Chem. 2023;140:106832. doi: 10.1016/j.bioorg.2023.106832

[18] Le TS, Takahashi M, Isozumi N, et al. Quick and mild isolation of intact lysosomes using magnetic–plasmonic hybrid nanoparticles. ACS Nano. 2022;16(1):885–896. doi: 10.1021/acsnano.1c08474

[19] Zhitomirsky B, Farber H, Assaraf YG. LysoTracker and MitoTracker red are transport substrates of P-glycoprotein: implications for anticancer drug design evading multidrug resistance. J Cellular Mol Medi. 2018;22(4):2131–2141. doi: 10.1111/jcmm.13485

[20] Valm AM, Cohen S, Legant WR, et al. Applying systems-level spectral imaging and analysis to reveal the organelle interactome. Nature. 2017;546(7656):162–167. doi: 10.1038/nature22369

[21] Zhu H, Fan J, Du J, et al. Fluorescent probes for sensing and imaging within specific cellular organelles acc. Chem Res. 2016;49:2115–2126. doi: 10.1021/acs.accounts.6b00292

[22] Tamura T, Fujisawa A, Tsuchiya M, et al. Organelle membrane-specific chemical labeling and dynamic imaging in living cells. Nat Chem Biol. 2020;16(12):1361–1367. doi: 10.1038/s41589-020-00651-z

[23] Miyata K, Christie RJ, Kataoka K. Polymeric micelles for nano-scale drug delivery. React Funct Polym. 2011;71(3):227–234. doi: 10.1016/j.reactfunctpolym.2010.10.009

[24] Osada K, Christie RJ, Kataoka K. Polymeric micelles from poly(ethylene glycol)–poly(amino acid) block copolymer for drug and gene delivery. J R Soc Interface. 2009;6(suppl_3):S325–39. doi: 10.1098/rsif.2008.0547.focus

[25] Loomis K, Smith B, Feng Y, et al. Specific targeting to B cells by lipid-based nanoparticles conjugated with a novel CD22-ScFv. Exp Mol Pathol. 2010;88(2):238–249. doi: 10.1016/j.yexmp.2010.01.006

[26] Chen WC, Sigal DS, Saven A, et al. Targeting B lymphoma with nanoparticles bearing glycan ligands of CD22. Leukemia Lymphoma. 2012;53(2):208–210. doi: 10.3109/10428194.2011.604755

[27] Shan D, W PO. Constitutive endocytosis and degradation of CD22 by human B cells. J Immunol. 1995;154(9):4466–4475. doi: 10.4049/jimmunol.154.9.4466

[28] O'reilly MK, Tian H, Paulson JC. CD22 is a recycling receptor that can shuttle cargo between the cell surface and endosomal compartments of B cells. J Immunol. 2011;186(3):1554. doi: 10.4049/jimmunol.1003005

[29] Morschhauser F, Flinn IW, Advani R, et al. Polatuzumab vedotin or pinatuzumab vedotin plus rituximab in patients with relapsed or refractory non-Hodgkin lymphoma: final results from a phase 2 randomised study (ROMULUS). Lancet Haematol. 2019;6(5):e254–65. doi: 10.1016/S2352-3026(19)30026-2

[30] Giltiay NV, Shu GL, Shock A, et al. Targeting CD22 with the monoclonal antibody epratuzumab modulates human B-cell maturation and cytokine production in response to Toll-like receptor 7 (TLR7) and B-cell receptor (BCR) signaling. Arthritis Res Ther. 2017;19(1):91. doi: 10.1186/s13075-017-1284-2

[31] Li J, Wei M-M, Song Q, et al. Anti-CD22 epratuzumab for systemic lupus erythematosus: a systematic review and meta-analysis of randomized controlled trials. Exp Ther Med. 2019;18:1500–1506. doi: 10.3892/etm.2019.7630

[32] Lin AY, Dinner SN. Moxetumomab pasudotox for hairy cell leukemia: preclinical development to FDA approval. Blood Adv. 2019;3(19):2905-2910 doi: 10.1182/bloodadvances.2019000507

[33] Nobre CF, Newman MJ, A D, et al. Moxetumomab pasudotox-tdfk for relapsed/refractory hairy cell leukemia: a review of clinical considerations. Cancer Chemother Pharmacol. 2019;84(2):255–263. doi: 10.1007/s00280-019-03875-6

[34] Green MR, Sambrook J, Sambrook J. Molecular cloning: a laboratory manual. Cold Spring Harbor, N.Y: Cold Spring Harbor Laboratory Press; 2012.

[35] Pastan IH, Salvatore G, Beers R, et al. inventors; US Department of Health and Human Services, assignee. Mutated Anti-CD22 antibodies with increased affinity to CD22-expressing leukemia cells. United States patent US. 2009/0004734 A1. 2009 Jan 1.

[36] Salvatore G, Beers R, Margulies I, et al. Improved cytotoxic activity toward cell lines and fresh leukemia cells of a mutant anti-CD22 immunotoxin obtained by antibody phage display. Clin Cancer Res. 2002;8 (4):995–1002.

[37] Yu S-F, Zheng B, Go M, et al. A novel anti-CD22 anthracycline-based antibody–drug conjugate (ADC) that overcomes resistance to auristatin-based ADCs. Clin Cancer Res. 2015;21(14):3298–3306. doi: 10. 1158/1078-0432.CCR-14-2035

[38] Ereño-Orbea J, Sicard T, Cui H, et al. Molecular basis of human CD22 function and therapeutic targeting. Nat Commun. 2017;8(1):764. doi: 10.1038/s41467-017-00836-6

[39] Roy G, Reier J, Garcia A, et al. Development of a high yielding expression platform for the introduction of non-natural amino acids in protein sequences. MAbs. 2020;12(1):1684749. doi: 10.1080/19420862.2019. 1684749

[40] St A, H A, Huang F, et al. A reactive antibody platform for one-step production of antibody–drug conjugates through a diels–alder reaction with Maleimide. Bioconjugate Chem. 2019;30(9):2340–2348. doi: 10. 1021/acs.bioconjchem.9b00436

[41] Urello MA, Xiang L, Colombo R, et al. Metabolite-based modification of Poly(l -lysine) for improved gene delivery. Biomacromolecules. 2020;21 (9):3596–3607. doi: 10.1021/acs.biomac.0c00614

[42] Anon Lysosome triggered near-infrared fluorescence imaging of cellular trafficking processes in real time - PMC.

[43] Florinas S, Liu M, Fleming R, et al. A nanoparticle platform to evaluate bioconjugation and receptor-mediated cell uptake using cross-linked polyion complex micelles bearing antibody fragments. Biomacromolecules. 2016;17 (5):1818–1833. doi: 10.1021/acs.biomac.6b00239

[44] Kemmer GC, Bogh SA, Urban M, et al. Lipid-conjugated fluorescent pH sensors for monitoring pH changes in reconstituted membrane systems. Analyst. 2015;140(18):6313–6320. doi: 10.1039/ C5AN01180A

[45] Du X, Beers R, FitzGerald DJ, et al. Differential cellular internalization of anti-CD19 and -CD22 immunotoxins results in different cytotoxic activity. Cancer Res. 2008;68 (15):6300. doi: 10.1158/0008-5472.CAN-08-0461

[46] Collins BE, Blixt O, Han S, et al. High-affinity ligand probes of CD22 overcome the threshold set by cis ligands to allow for binding, endocytosis, and killing of B cells. J Immunol. 2006;177(5):2994–3003. doi: 10. 4049/jimmunol.177.5.2994

[47] S IG, J SS. DropArray™, a wall-less 96-well plate for uptake and Immunofluorescence Microscopy, confirms CD22 recycles. Traffic. 2014;15(3):255–272. doi: 10.1111/tra.12144

[48] Grant BW, Jung S-H, Johnson JL, et al. A phase 2 trial of extended induction epratuzumab and rituximab for previously untreated follicular lymphoma: CALGB 50701: Rituximab+Epratuzumab in follicular NHL. Cancer. 2013;119(21):3797–3804. doi: 10.1002/ cncr.28299

[49] Raetz EA, Cairo MS, Borowitz MJ, et al. Re-induction chemoimmunotherapy with epratuzumab in relapsed acute lymphoblastic leukemia (ALL): phase II results from Children's Oncology Group (COG) study ADVL04P2: Re-induction with epratuzumab in relapsed ALL. Pediatr Blood Cancer. 2015;62 (7):1171–1175. doi: 10.1002/pbc.25454

[50] Kraeber-Bodere F, Pallardy A, Maisonneuve H, et al. Consolidation anti-CD22 fractionated radioimmunotherapy with 90 Y-epratuzumab tetraxetan following R-CHOP in elderly patients with diffuse large B-cell lymphoma: a prospective, single group, phase 2 trial. Lancet Haematol. 2017;4(1):e35–45. doi: 10. 1016/S2352-3026(16)30168-5

[51] Strauss SJ, Morschhauser F, Rech J, et al. Multicenter phase II trial of immunotherapy with the humanized anti-CD22 antibody, Epratuzumab, in combination with Rituximab, in refractory or recurrent Non-Hodgkin's lymphoma. JCO. 2006;24(24):3880–3886. doi: 10.1200/JCO.2006.05.6291

[52] Kreitman RJ, Tallman MS, Robak T, et al. Phase I trial of anti-CD22 recombinant immunotoxin moxetumomab pasudotox (CAT-8015 or HA22) in patients with hairy cell leukemia. JCO. 2012;30(15):1822–1828. doi: 10.1200/JCO.2011.38.1756

[53] Dhillon S. Moxetumomab Pasudotox: first global approval. Drugs. 2018;78(16):1763–1767. doi: 10. 1007/s40265-018-1000-9

[54] Kreitman RJ, Pastan I. Antibody fusion proteins: anti-CD22 recombinant Immunotoxin Moxetumomab Pasudotox. Clin Cancer Res. 2011;17(20):6398–6405. doi: 10.1158/1078-0432.CCR-11-0487

[55] Carnahan J, Wang P, Kendall R, et al. Epratuzumab, a humanized monoclonal antibody targeting CD22: characterization of in vitro properties. Clin Cancer Res. 2003;9:3982S–3990S.

[56] Li D, Poon KA, S-F Y, et al. DCDT2980S, an anti-CD22-monomethyl Auristatin E Antibody–Drug Conjugate, is a potential treatment for Non-Hodgkin Lymphoma. Mol Cancer Ther. 2013;12(7):1255–1265. doi: 10.1158/1535-7163.MCT-12-1173

[57] G PA, Williams M, Gray AM, et al. Anti-CD22-MCC-DM1: an antibody-drug conjugate with a stable linker for the treatment of non-Hodgkin's lymphoma. Leukemia. 2010;24(9):1566–1573. doi: 10.1038/leu. 2010.141

[58] St A, H A, Huang F, et al. A diene-containing noncanonical amino acid enables dual functionality in proteins: rapid diels–alder reaction with maleimide or proximity-based dimerization. Angew Chem Int Ed. 2019;58 (25):8489–8493. doi: 10.1002/anie.201903494

[59] Takahashi A, Suzuki Y, Suhara T, et al. In situ cross-linkable hydrogel of hyaluronan produced via

copper-free click chemistry. Biomacromolecules. 2013;14(10):3581–3588. doi: 10.1021/bm4009606

[60] Smith RM, Jarett L. Differences in adenosine triphosphate dependency of receptor-mediated endocytosis of α2-macroglobulin and insulin correlate with separate routes of ligand-receptor complex internalization*. Endocrinology. 1990;126(3):1551–1560. doi: 10.1210/endo-126-3-1551

[61] Mauvezin C, Neufeld TP. Bafilomycin A1 disrupts autophagic flux by inhibiting both V-ATPase-dependent acidification and Ca-P60A/SERCA-dependent autophagosome-lysosome fusion. Autophagy. 2015;11(8):1437. doi: 10.1080/15548627. 2015.1066957

[62] Harlan FK, Lusk JS, Mohr BM, et al. Fluorogenic substrates for visualizing acidic organelle enzyme activities. PLOS ONE. 2016;11(5):e0156312. doi: 10. 1371/journal.pone.0156312

[63] Xu M, Liu K, Swaroop M, et al. A phenotypic compound screening assay for lysosomal storage diseases. J Biomol Screen. 2014;19(1):168–175. doi: 10.1177/ 1087057113501197

[64] Cheng Y, Qu Z, Jiang Q, et al. Functional materials for subcellular targeting strategies in cancer therapy: progress and prospects. Adv Mater. 2023:e2305095. doi: 10.1002/adma.202305095

[65] Shao X, Meng C, Song W, et al. Subcellular visualization: organelle-specific targeted drug delivery and discovery. Adv Drug Deliv Rev. 2023;199:114977. doi: 10.1016/j.addr.2023.114977

[66] Hong J, Zhang J, Li Q, et al. One stone, three birds: a smart single fluorescent probe for simultaneous and discriminative Imaging of lysosomes, lipid droplets, and mitochondria. Anal Chem. 2023;95(5):2671–2679. doi: 10.1021/acs.analchem.2c03073

[67] Day RA, Sletten EM. Experimental perspectives on direct visualization of endosomal rupture. Chem bio chem. 2021;22(23):3277–3282. doi: 10.1002/cbic.202100379

[68] Zheng F, Ma Y, Ding J, et al. Ratiometric and discriminative visualization of autophagic processes with a novel dual-responded lysosome-specific fluorescent probe. Biomater Res. 2023;27(1):66. doi: 10.1186/ s40824-023-00409-3

[69] Miyazaki T, Chen S, Florinas S, et al. A hoechst reporter enables visualization of drug engagement in vitro and in vivo: toward safe and effective nano-drug delivery. ACS Nano. 2022;16(8):12290–12304. doi: 10.1021/acsnano.2c03170